

Volume 57

http://acousticalsociety.org/



#### NOVEM2025

### **NOise and Vibration Emerging Methods**

Garmisch-Partenkirchen, Germany
6-8 May 2025

Structural Acoustics and Vibration: Developments in Vibroacoustics

# Structural intensity assessment of experimental structural response data from aircraft structures

#### Sebastian Florens Zettel, René Winter and Marc Böswald

Institute of Aeroelasticity, German Aerospace Center DLR Site Göttingen: Deutsches Zentrum fur Luft-und Raumfahrt DLR Standort Gottingen, Göttingen, Lower Saxony, 37073, GERMANY; sebastian.zettel@dlr.de; rene.winter@dlr.de; marc.boeswald@dlr.de

### **Marcus Maeder and Steffen Marburg**

Chair of Vibro-Acoustics of Vehicles and Machines, Technical University Munich: Technische Universitat Munchen, Munich, GERMANY; marcus.maeder@tum.de; steffen.marburg@tum.de

Structural intensity allows the user to visualize the vibrational power flow in structures. With appropriate post-processing, it is also possible to identify sinks and sources in vibrating structures. This circumstance ideally allows us to perform assessments of possible placements of countermeasures. While it is trivial to calculate the structural intensity via numerical simulations, this is not the case for measurement data, as crucial information regarding non-measurable degrees of freedom is missing. This publication overviews a methodology to acquire structural intensity vector fields from measurement data, and the results of two structural intensity assessments based on measurement data of aircraft structures are presented. Furthermore, a comprehensive outlook is given that focuses on a novel path identification approach currently in development and other crucial factors that need investigation to conduct structural intensity assessments at a state-of-the-art level for research and industry.



#### 1. INTRODUCTION

The goal of structural intensity (STI) analyses of experimentally acquired structural response data is to assess vibration propagation, as it allows visualization and quantification of the vibrational power flow in terms of direction and magnitude for thin-walled structures. Aircraft structures experience excitations from multiple vibration sources, i.e., engines and subsystems. These vibrations propagate throughout the structure and partially contribute to noise emission into the cabin cavity and vibration loads in the seats. Therefore, identifying sources and sinks as well as the paths between them helps ideally with applying countermeasures. For example, in the form of damping patches, the principle of constrained layer damping is used. Of special interest is the ability to quantify the power input into a structure and the power that remains at critical areas of the structure far away from the excitation. The effects of installed countermeasures can be quantified in terms of vibrational energy transfer before and after installation.

In 2018, Biedermann et al. [1] presented the idea of using a hybrid method that utilizes the finite element method (FEM) approach of calculating forces in elements to estimate the STI from structural response data. The advantage of this method is the use of elements and their shape functions to calculate the elemental forces in the centroids and estimate the missing nodal rotations, which cannot be measured easily in experiments. Additionally, the FEM calculation process is performed in local element coordinate systems, which allows the evaluation of structures with arbitrarily shaped surfaces. Especially for aircraft structures, this is a major advantage, as the respective structures, i.e., wings and fuselages, are rarely academic textbook structures.

After first tests on laboratory structures, i.e., plate structures [1], the hybrid method was also applied to datasets of large-scale structural response datasets of aircraft structures [2] [3]. This paper provides an overview of two of these evaluations. The first covers the structural intensity analysis of the German Aerospace Center (DLR) research aircraft ISTAR's fuselage conducted in 2022. The second focuses on the evaluation of a A320 wing, which was tested under laboratory conditions in 2023. Furthermore, an overview is given, showing the current focus of development and future applications with other industry partners to establish STI as a valuable analysis tool.

Section 2 covers the fundamentals of STI and provides a short description of the hybrid method. In section 3, evaluations of the aircraft structures are presented and discussed. Section 4 provides an overview of the ongoing developments regarding STI at the DLR.

# 2. ESTIMATING STRUCTURAL INTENSITY FROM EXPERIMENTAL DATA

STI allows visualization and quantification of the vibrational power flow per cross-sectional area in thin-walled structures. The STI is presented in the form of a vector, showing the direction and magnitude at a specific location of the structure under investigation. A basic understanding of how the STI works can be acquired by looking at the instantaneous sound intensity [4]

$$\vec{I}_{fluid,t} = p \begin{bmatrix} \dot{u} \\ \dot{v} \\ \dot{w} \end{bmatrix}. \tag{1}$$

with the scalar pressure p and the particle velocity vector  $(\dot{u}, \dot{v}, \dot{w})$ . The sound intensity describes the directed sound power per area at a certain distance from the source. Transferring this approach to solid structures, the pressure value p is replaced by the full stress tensor S for solid materials

$$\vec{I}_{solid,t} = -\mathbf{S} \cdot \begin{bmatrix} \dot{u} \\ \dot{v} \\ \dot{w} \end{bmatrix} = - \begin{bmatrix} \sigma_{xx} & \tau_{xy} & \tau_{xz} \\ \tau_{yx} & \sigma_{yy} & \tau_{yz} \\ \tau_{zx} & \tau_{zy} & \sigma_{zz} \end{bmatrix} \begin{bmatrix} \dot{u} \\ \dot{v} \\ \dot{w} \end{bmatrix}. \tag{2}$$

with the normal stress  $\sigma$  and the shear stress  $\tau$  [4].

Using common measurement techniques, i.e., laser doppler vibrometer, accelerometers and digital image correlation, it is not possible to acquire the full stress and velocity fields of solid materials, as the measurement is only performed on the surface of the structure. Accordingly, the STI is often calculated for thin-walled

structures. In that case, the z-components of the stress tensor are neglected. In addition to solid materials, thin-walled structures also experience flexural deformation, and according to internal forces, i.e., bending moments, emerge. Additionally, STI evaluations are typically performed in the frequency domain. Therefore, equation Eq. (2) is adapted for the calculation of the STI in thin-walled structures by using internal forces, i.e., normal forces N, transverse forces Q and bending moments M, as well as complex conjugated values indicated by a star superscript [5]

$$\vec{I}_{plate,f} = -\frac{1}{2hb} Re \left\{ \begin{bmatrix} N_x & N_{xy} & Q_{xz} \\ N_{yx} & N_y & Q_{yz} \\ 0 & 0 & 0 \end{bmatrix} \begin{bmatrix} \dot{u}^* \\ \dot{v}^* \\ \dot{w}^* \end{bmatrix} + \begin{bmatrix} M_{xy} & M_x & 0 \\ M_y & M_{yx} & 0 \\ 0 & 0 & 0 \end{bmatrix} \begin{bmatrix} \omega_x^* \\ \omega_y^* \\ \omega_z^* \end{bmatrix} \right\}. \tag{3}$$

The variables h and b describe the height and width of the cross-sectional area in the flow direction. The factor  $\frac{1}{2}$  and the  $Re(\cdot)$  operator arise from the relationship between time- and frequency-domain products  $\langle q_{t1} \ q_{t2} \rangle t = \frac{1}{2} Re\{q_{f1} \ q_{f2}^*\}$  according to Verheij et al. [6] with the time average  $\langle \cdot \rangle t$  and the placeholder for any time-domain value  $q_t$  and frequency-domain value  $q_f$ .

#### A. HYBRID METHOD FOR ESTIMATING STRUCTURAL INTENSITY

To estimate the STI from structural response data acquired from measurements, it is necessary to calculate internal plate forces and estimate the angular velocities at the assessment location. The eight-sensor method described by Pavic et al. [7] allows us to acquire the missing plate forces by using the fundamental plate equations. However, this method is not applicable to arbitrary surfaces but only flat surfaces or surfaces for which a curvilinear coordinate system can be constructed. Additionally, as name states, eight measurement positions are necessary to calculate one STI vector. The *hybrid method*, which uses the FEM approach to calculate element forces, overcomes these limitations. This method allows us to evaluate the STI on arbitrarily shaped surfaces with only four necessary data points via quadrilateral shell elements. This section covers the basic idea and working principles behind the hybrid method. A comprehensive description of the hybrid method is beyond the scope of this paper. For a more detailed analysis, see Biedermann et al. [1].

The steps to perform a FE simulation are as follows:

- 1. Create geometry
- 2. Choosing the element type
- 3. Spatial discretization
- 4. Set material properties
- 5. Build system matrices
- 6. Set boundary conditions
- 7. Response analysis (Results: Nodal displacement and rotations)
- 8. Calculate element forces and moments in centroids

Setting up the FE simulation allows us to solve the system, and the results are the nodal displacements and rotations. These are used to calculate the forces in the element centroids. Accordingly, the STI can be calculated easily, as all necessary data are available in reference to Eq. (3). The geometry is already known from the respective measurement location points. Typically, the measurement grid is set as quadrilateral four-node shell elements. Accordingly, the geometry is discretized, and bilinear shape functions can be set up. The material parameters need to be known in the form of Young's modulus E, density  $\rho$  and Poisson's ratio  $\nu$  when considering isotropic materials. The nodal displacement is the measured response acquired during the measurement at each point of the mesh. To calculate the element forces in the centroids according to the material law for plates, only the nodal rotations are missing. Nodal rotations are difficult to measure, especially on large arbitrarily shaped surfaces. The hybrid method utilizes the bilinear shape functions  $\mathcal N$  and their partial derivatives along the coordinate axes to estimate the nodal rotations  $\varphi$  from the nodal displacements w by [1]

$$\varphi_{x} = \frac{\partial w}{\partial y} = \left\{ \frac{\partial \mathcal{N}_{1}}{\partial y} \quad \dots \quad \frac{\partial \mathcal{N}_{m}}{\partial y} \right\} \left\{ w_{1} \quad \dots \quad w_{M} \right\}^{T}, \tag{4}$$

$$\varphi_{y} = -\frac{\partial w}{\partial x} = -\left\{\frac{\partial \mathcal{N}_{1}}{\partial x} \quad \dots \quad \frac{\partial \mathcal{N}_{m}}{\partial x}\right\} \{w_{1} \quad \dots \quad w_{M}\}^{T}.$$
(5)

The FEM allows all necessary calculations to be performed in a local elemental coordinate system. Therefore, the hybrid method automatically enables STI calculations to be performed on arbitrarily shaped surfaces. By knowing the nodal displacements and rotations as well as the material law and material parameters, the elemental forces can be calculated. Therefore, all necessary information exists to calculate the STI according to Eq. (3).

# 3. STRUCTURAL INTENSITY EVALUATION OF AIRCRAFT STRUCTURES

In two recent projects, DLR applied the hybrid method to aircraft structures. This section covers the experimental setup of both measurement campaigns. Afterwards, the calculated STI vector fields and the insights drawn from them are discussed.

#### A. FUSELAGE OF THE ISTAR RESEARCH AIRCRAFT

The following description is a rephrased summary of the publication from Winter et al. [8]. The DLR research aircraft ISTAR is a Falcon 2000LX with a fuselage length of 20.2 m and a cabin width of 2.35 m (see Figure 1 a). In 2022, a measurement campaign was performed on the aircraft. The main focus of the campaign was to capture the structural response of the fuselage during shaker excitation in a frequency range of 40–500 Hz to perform model updating on a FE model of the aircraft and to estimate the vibrational power flow in the structure. Additionally, the fuselage response near the engines during excitation by the running engines was of interest. This publication only covers the main points of fuselage excitations with shakers.

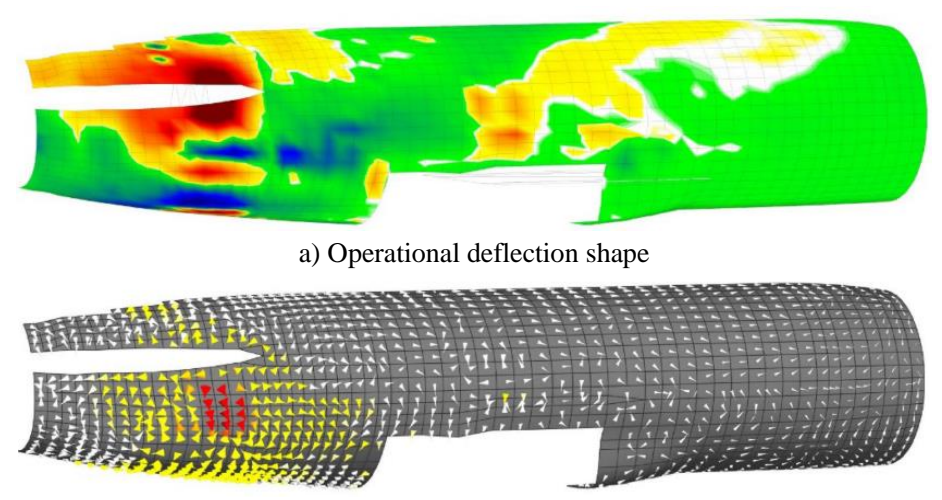


Figure 1. Dassault Falcon 2000LX [8] a) and sensor configuration for measuring the aircraft vibration [8] b)

The sensor configuration for the shaker excitation in Figure 1 b) covers the full length of the fuselage but only one half of the circumference. A total of 1300 points were measured. However, for the actual measurement, only a subset of 300 accelerometers was used. The sensor configuration shows the full measurement grid with the first set of measurement locations accessed with the available accelerometers in yellow. A detailed description of the measurement can be found in Winter et al. [9].

The results of the measured response for a shaker excitation on the pylon are presented in Figure 2 a) for the 100 Hz 1/3-octave band. The excitation was performed with a shaker acting on the pylon (rear narrow cut-out section in the deflection shape) toward its leading edge. The deflection is presented with a diverging colormap ranging from white over yellow to red for outward deflections and white over green to blue for inward deflections. Accordingly, the fuselage structure in the tail section experiences strong responses just below the

pylon cut-out. Additionally, a window section above the wing clearly shows resonant behavior. Extracting any information related to power flows from the response field alone would be nearly impossible. In terms of STI evaluations, a vector plot showing the divergence component of the STI vector field is presented in Figure 2 b). The vector field is displayed via normalized vectors with a colormap ranging from white over yellow to red. The hybrid method, outlined in section 2, was used to calculate the STI on the basis of the given operational deflection shape. The goal was to identify sources, sinks and paths in STI fields. In the case of the 100 Hz 1/3-octave band, the tail section of the fuselage below the pylon shows a characteristic power flow field with a distinctive sink. The structural response above the pylon section does not seem to result in a particular strong power flow. After evaluating the aircraft structure and the installed subsystems inside, it was found that in the section below the pylon, an oil pump is installed, which represents a relatively heavy point mass. Therefore, vibrations originating from the shaker and propagating throughout the pylon in the fuselage are partially attenuated in this area. A clear source cannot be identified, but the surrounding area of the front half of the pylon cut-out in the fuselage tail section has higher STI magnitudes than does the back half of the pylon. This finding indicates that the front half of the pylon excites the fuselage structure in general. A clear path was only identifiable between the pylon cut-out and the sink mentioned before. More STI-related results can be found in the full article of Winter et al. [8].



b) Divergence component of STI vector field

Figure 2. Operational deflection shape and divergence vector field of the decomposed STI vector field for the 100 Hz 1/3-order band (89–112 Hz) for shaker excitation on pylon [8]

#### **B. WING STRUCTURE OF AN A320 WING**

The following description is a rephrased summary of the publication from Norambuena et al. [10]. In 2023, the DLR performed a measurement campaign on a A320 wing under laboratory conditions. The decommissioned wing from the 1990s was set up in a hall at Airbus in Bremen with a support structure (see Figure 3). The support structure allows the wing to be installed in a manner that is commonly performed on the aircraft itself. The goal of the campaign was to capture the structural response along the full wing for model updating of a respective FE model. Furthermore, the goal was to capture the structural response in specific areas of the wing to perform an STI analysis regarding the transferred power flow in the wing structure.



Figure 3. A320 wing attached to the wing support structure; red box: support structure [10]

In the case of the structural response measurement along the full length of the wing, accelerometers were installed on the leading and trailing edges as well as in the centerline of the wing, as shown by the black markers in Figure 4. The spacing of the sensors was chosen to capture the wavelengths of the first five eigenfrequencies. Sensors in the centerline were installed to differentiate between the bending and torsion modes. The sensor configuration for the STI evaluation has a relatively high density, see red markers in Figure 4. Accelerometers for the STI measurement were installed on the top and bottom surfaces of the wing in two areas. The 'root section' was chosen to capture the power flow transferred into the support structure, and the 'pylon section' was chosen to capture the power input into the wing as the excitation was performed in the pylon section. The sensor density allows the capture of wavelengths up to 400 Hz, according to a study performed with the FE model of the wing considering six elements per wavelength.

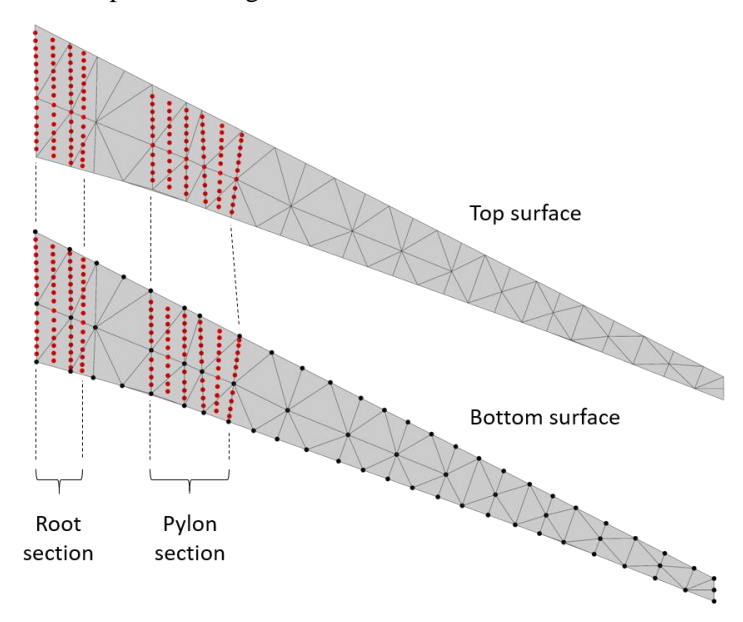


Figure 4. Sensor layout for vibration measurement; red: structural intensity grid; black: modal analysis grid [10]

In Figure 5, the areas for the sensor configuration are presented in the form of meshes consisting of fournode elements using the accelerometer locations as nodes. In the root section, the gray area represents the line of elements that is used to calculate the power that is transferred into the support structure. The blue markers indicate the locations of the engine attachment points on the bottom surface of the wing. The forward and aft attachment points are the two hard points (structurally stiff points for load introduction) of the wing on which the engine is attached. In the case of the measurement campaign, these points were used to introduce a realistic load profile of engine vibrations with the multiaxial excitation system (MAES). This system allows the excitation of structures with a predefined multiaxial load profile using at least two shakers simultaneously; see section 4 in Norambuena et al. [10] for a detailed description of the MAES.

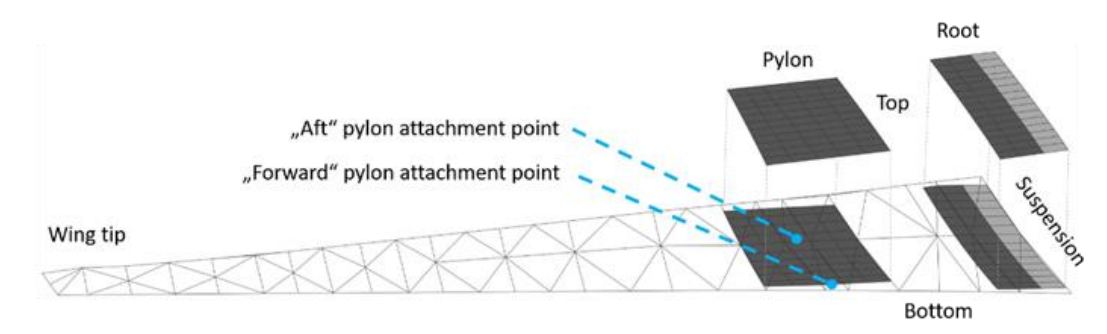


Figure 5. STI assessment areas (gray) and pylon attachment points in relation to the lower wing surface [10]

The STI vector fields in Figure 6 were calculated for two excitation setups. A generic excitation using a single shaker on the hard points with a pseudorandom excitation and a load profile using the MAES system. The pseudorandom excitation was used for the vibroacoustic characterization of the wing in terms of the eigenfrequencies. However, these excitations were also interesting to evaluate for comparison with the MAES system. In Figure 6 a), the excitation on the leading-edge results in a STI field with random directions. The excitation location is close to the front spar of the wing (stiff beam-like structure carrying the flight loads and the wing weight on the ground). Therefore, vibrations seem to propagate mainly along the spar and do not introduce a meaningful STI flow in the rest of the measurement patches. This changes for an excitation at the aft engine attachment hard-point; see Figure 6 b). Originating from the excitation location, STI clearly flows toward the root of the wing and its tip on the bottom surface of the wing. The flow toward the tip shows higher STI magnitudes according to the normalized vector field.

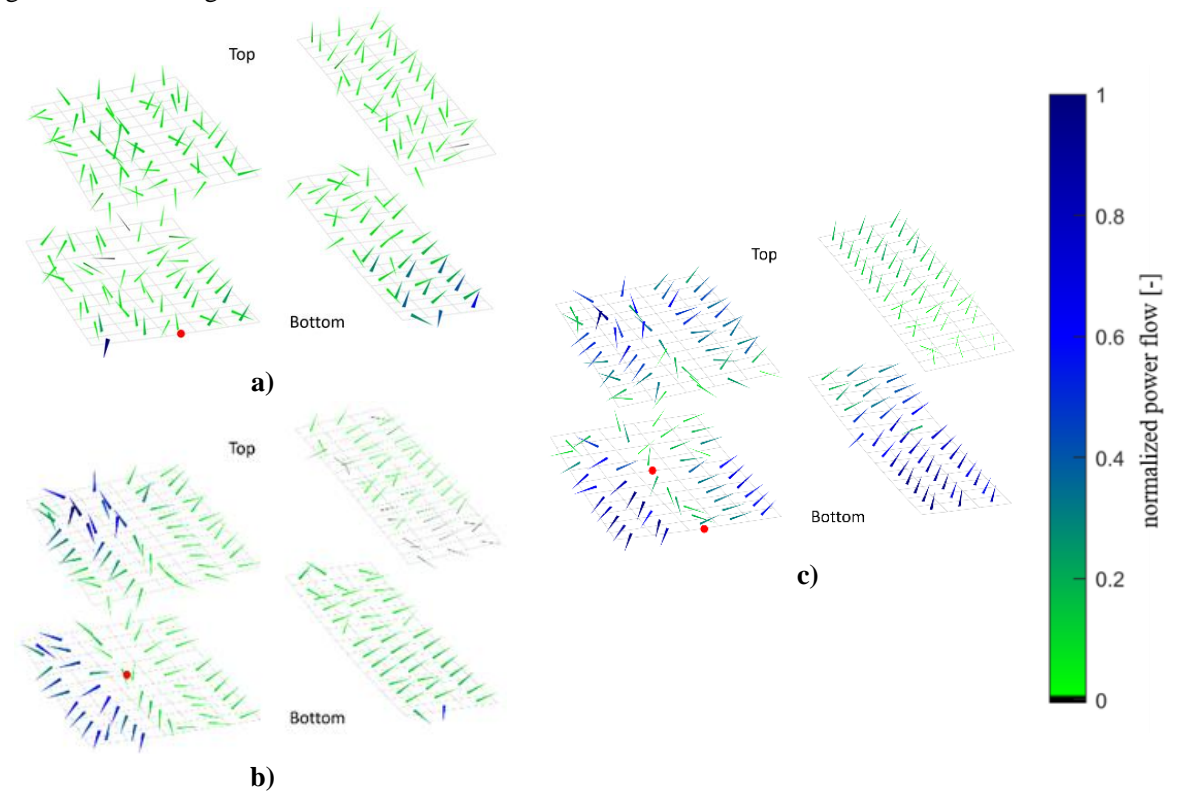


Figure 6. Vector fields for generic pseudorandom excitation: at leading a) and trailing b) edges, compared with MAES excitation c) at engine frequency N1 (70 Hz); color scale: normalized to maximum power in the respective fields [10]

The vibrations also propagate into the top surface of the wing, and the STI vector field shows a flow in both wing directions. The resulting STI flow on the top surface in the root sections is smaller than that in the bottom section; therefore, the main power flow seems to remain on the bottom surface of the wing. For the MAES excitation, both excitation points are used simultaneously. The normalized STI vectors have large magnitudes on the bottom surface of the wing, also flowing into the support structure on the right. While the vibrations again also propagate into the top surface of the wing and the STI flows in both wing directions, the resulting power flow into the support structure is smaller than that on the bottom surface.

In the case of the STI vector fields calculated on the basis of the structural response acquired with the MAES excitation, the power flow at the wing support structure was quantified. The power input was calculated on the basis of the driving point force and velocity measured with an impedance head by [10]

$$P_{excitation,f} = \frac{1}{2} Re\{F \cdot \dot{v}^*\}. \tag{6}$$

The power flow over the wing root into the support structure was calculated via a line integral integrating the STI magnitudes, which flow perpendicular to the last line of elements in the root section on the top and bottom surfaces. Figure 7 presents a comparison of the excitation power from the shaker system and the transmitted power at the root of the wing. The four frequencies  $0.5 \times N1$ , N1,  $2 \times N1$  and N2 refer to specific engine rotation frequencies for which load profiles were calculated (see Zettel et al. [11]), which are the MAES used to excite the structure. The exact frequencies of N1 and N2 cannot be determined, but they are close to 70 Hz and 200 Hz, respectively. Over all frequencies, the transmitted power at the wing root is smaller than the injected excitation power. Power is dissipated throughout the structure, and less power leaves the system through the root than is injected. The ratio between the injected and transmitted power varies over the frequency, which shows that certain frequencies result in STI power flows that transmit the power more efficiently through the structure. The small power values may seem odd at the first view, but evaluations of beam structures conducted by Hambric et al. [12] resulted in power flows at similar orders of magnitude.

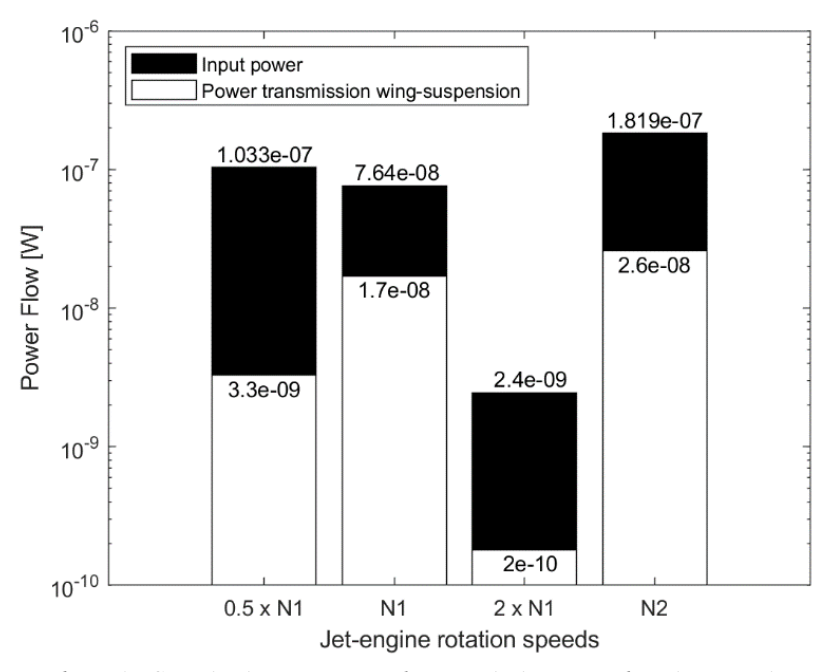


Figure 7. Power input by MAES excitation system and transmission over the wing root into the suspension [10]

#### 4. ONGOING DEVELOPMENTS

Currently, the main focus of ongoing research regarding STI at DLR is explicit path identification. Several publications in recent decades have aimed to identify paths between sources and sinks using the divergence component of decomposed STI vector fields [13] [14] [15] [16] [17]. Path identification was performed by engineering judgment. A dedicated methodology to determine paths does not exist thus far. In a study presented

at the DAGA conference in 2024 by Zettel et al. [18], the first results of an approach for path identification methodology were shown. The following paragraphs are a summary of this publication.

Considering a STI vector field calculated from the structural response of a simple quadratic plate, the decomposed vector field components for divergence and rotation can be acquired via Hodge Helmholtz decomposition. The FE model of the plate used for the evaluation is simply supported with dimensions of 1 m by 1 m and a thickness of 1 mm. The plate model was discretized with  $60 \times 60$  elements, and material parameters for aluminum, i.e., Young's modulus of 70 MPa, density of 2700 kg/m³ and Poisson's ratio of 0.34, were used. The excitation consists of a point force of 1 N normal to the surface at the location x = 0.266 m and y = 0.2 m. A dashpot damper was used for local dissipation at the locations x = 0.733 m and y = 0.8 m with a viscous damping value of 1000 N/m/s. In Figure 8, components of a vector field decomposition are presented for increasing frequency from top to bottom in the range of 210-260 Hz with 10 Hz steps. Green and blue indicate the source and sink areas for the divergence component a), respectively. In the case of the rotational component b), the green and blue areas indicate the mathematical positive and negative vortex spin directions, respectively. For a fixed excitation source in the form of a point force on the plate, the divergence component does not vary significantly over frequency. The source location and distribution of the potential field remain more or less constant. This is not the case for the rotational component. The potential field changes continuously over frequency and is rarely constant. The full STI vector field changes its characteristics continuously over frequency as well. The reason for the significant changes in the STI vector fields and the respective decomposed components is that both of them depend on the current operational deflection shape (ODS). The ODSs are dependent on the frequency and the sensitivity to frequency changes depend on the respective geometry and distribution of mass and stiffness. The full STI vector fields are assumed to contain the path information, and the components resulting from the decomposition need to contain it. Therefore, Zettel et al. [18] concluded that the rotational component of decomposed STI vector fields contains relevant information for explicit path identification, as only this potential field shows a similar frequency dependence to the STI field.

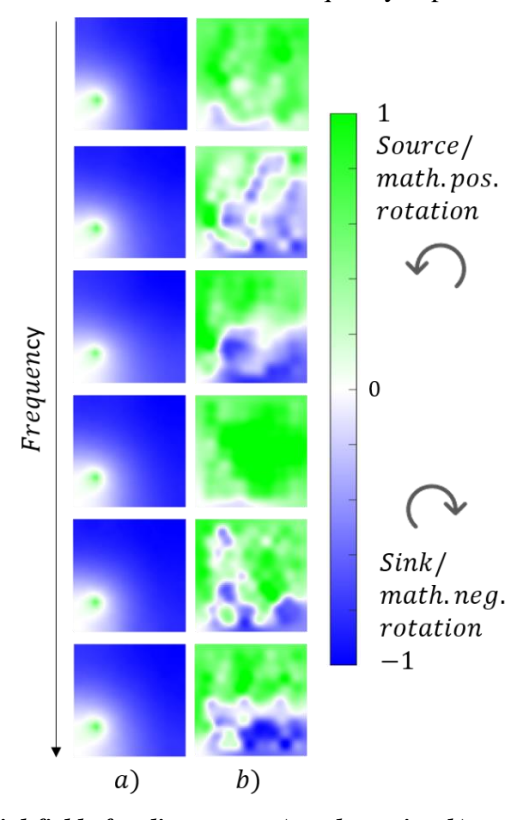


Figure 8. Comparison of potential fields for divergence a) and rotation b) components between 210 and 260 Hz with 10 Hz steps [18]

An open question is how the vortices of the rotational component can influence the formation of paths. Tanaka et al. [19] investigated vortices in STI vector fields. They reported that vortices form from operational deflection shapes formed by closely situated modes with similar energy levels (see Figure 9). The two modes

superpose each other and form an operational deflection shape with a phase relationship that forms a deflection pattern circulating around a local center.

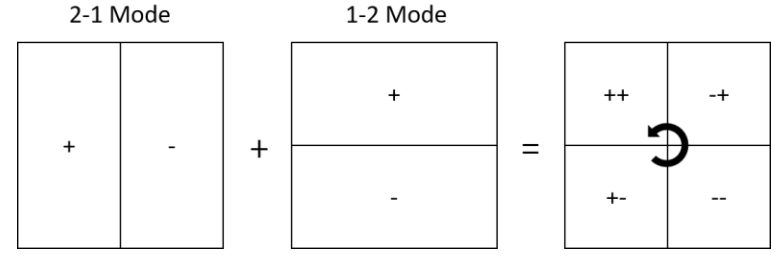


Figure 9. Fundamental vortex formation scheme from two modes [19]

Considering deflection shapes at higher frequencies, wavelengths become shorter, and therefore, the chance for a vortex to form increases. In cases of operational deflection shapes with short wavelengths, not just one vortex but multiple vortexes can form in the deflection shape and interact with each other. In terms of vortex interactions, there are two fundamental setups of vortex pairs to consider (see Figure 10). First, a vortex pair in which the individual vortex hubs have the same spin direction. This vortex pair forms a super vortex in which the two individual vortex hubs form a new hub. The second fundamental vortex pair consists of two individual vortex hubs with opposing spin directions. In this case, a vector field with a straight path between vortex hubs forms. The strengths of the individual vortex hubs in Figure 10 have the same strength. Therefore, an ideal super vortex forms for a vortex pair with the same spin direction, and the path is straight between the vortex pair and counterrotating spins. In the case of vortex hubs with different strengths, the super vortex for vortices with the same rotation speed would not be ideal, and a remaining flow between the vortex hubs would be present. For the counterrotating vortex pair, the path between them would not be ideally straight but would bend toward the vortex hub, which is stronger.

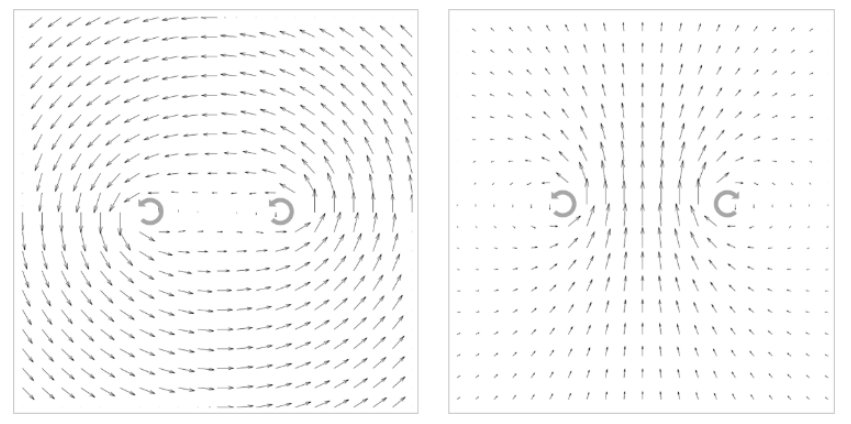


Figure 10. Fundamental vortex pair configuration, left: same spin direction, right: counterrotating spin direction

Considering the process of vortex formation described by Tanaka et al. [19] and the two fundamental vortex pair configurations described above, a hypothesis in terms of path identification on the basis of the rotational vector field component can be stated. Assuming that a finite number of vortex hubs are formed in an operational deflection shape, a network of interacting vortex hubs can form, which results in paths of vibrational energy throughout the structure.

Accordingly, Zettel et al. [18] proposed the hypothesis that the rotational component of STI vector fields is the basis for identifying paths of vibrational power flows. In particular, the transition regions between counterrotating areas in the rotational components should coincide with paths in the STI vector fields. However, there is also the possibility that transition regions in areas of rotation with the same spin direction hold path information. A respective publication proving this hypothesis is currently in work.

#### 5. SUMMARY AND OUTLOOK

A general-purpose evaluation tool for structural intensity analyses. Its capabilities include the estimation of structural intensity from measured structural response data, the quantification of power flows utilizing power balances and vector field decomposition. All this is possible on arbitrarily shaped surfaces. This allows the extension of the application capabilities from simple structures such as plates to more complex structures, e.g., aircraft fuselages and wings.

In terms of fuselage structures, the DLR performs structural intensity analyses on the fuselage structure of an aircraft of the private jet segment. The results provide initial insights into the capabilities of the tool and necessary improvements. Furthermore, an evaluation of a A320 wing under laboratory conditions was successfully performed. The structural intensity fields were evaluated, and a power balance was used. A novelty in both the field of structural intensity and aerospace engineering.

Current research focuses on the development of an explicit path identification methodology. With the help of vector field decompositions, it is possible to identify sources and sinks in structural intensity fields, but paths cannot be identified. Path identification is currently based on engineering judgment. The first approach, which is currently under further development, is based on the neglected rotational component of decomposed vector fields.

#### REFERENCES

- [1] J. Biedermann, R. Winter, M. Norambuena and M. Boeswald, "A hybrid numerical and experimental approach for structural intensity analysis of stiffened lightweight structures," in *ISMA*, Leuven, 2018.
- [2] R. Winter, J. Biedermann and M. W. M. Böswald, "Dynamic characterization of the A400M acoustics fuselage demonstrator," in *InterNoise*, Hamburg, Germany, 2016.
- [3] R. Winter, S. Heyen and M. Böswald, "Fully automated vibration measurements of aircraft fuselages in the mid-frequency range," in *ISMA*, Leuven, Belgium, 2018.
- [4] L. Cremer, M. Heckl and B. Petersson, Structure-Borne Sound, Berlin Heidelberg: Springer Verlag, 2005.
- [5] S. Hambric, "Power Flow and Mechanical Intensity Calculations in Structural Finite Element Analysis," *Journal of Vibration and Acoustics*, pp. 542-549, 1990.
- [6] J. Verheij, "Cross spectral density methods for measuring structure borne power flow on beams and pipes," *Journal of Sound and Vibration*, Bd. 70, Nr. 1, pp. 133-139, 1980.
- [7] G. Pavic, "Measurement of structure borne wave intensity, Part I: Formulation of the methods," *Journal of Sound and Vibration 49*, pp. 221-230, 1976.
- [8] R. Winter, M. Norambuena, J. Sinske and S.F. Zettel, "High-resolution vibroacoustic characterization of DLR's Falcon 2000LX ISTAR aircraft," *CEAS Aeronautical*, 2023.
- [9] R. Winter, M. Norambuena, J. Biedermann and M. Böswald, "Experimental characterization of vibro-acoustic properties of an aircraft fuselage," in *ISMA*, Leuven, Belgien, 2014.
- [10] M. Norambuena, S.F. Zettel, R. Dewald and R. Winter, "Experimental Vibroacoustic Characterization of an A320 Wing Utilizing a Controlled Shaker System for Artificial Engine-Vibration Excitation," in *Numerical Methods and Experimental Means for the Integration of Future Propulsion Systems A Resumé of the Achievements Made within the CleanSky 2 XDC Demonstrator*, Springer Nature Switzerland AG, 2025.
- [11] S.F. Zettel, M. Böswald, R. Winter and R. Dewald, "Jet engine vibration model for estimating pylon-wing interface loads for realistic structural excitation," *CEAS Aeronautical Journal*, 2025.
- [12] S. Hambric, "Comparison of experimental and finite element structure-borne flexular power measurements for a straight beam," *Journal of Sound and Vibration*, Bd. 170, Nr. 5, 1994.
- [13] B. Lamarsaude, Y. Bousseau and A. Jund, "Structural intensity analysis for car body design: going beyond interpretation issues through vector field processing," in *Proceedings of the ISMA 2014*, Leuven, Belgium, 2014.

- [14] F. Semperlotti and S. Conlon, "Structural damage identification in plates via nonlinear structural intensity maps," *Journal of the Acoustic Society of America*, Bd. 127, Nr. 2, 2010.
- [15] J. Wu, H. Zhu and Z. Yin, "Vibration power flow analysis of pipe perpendicular to plate structures," *Materials Science and Engineering*, Bd. 531, 2019.
- [16] J. Arruda and P. Mas, "Localizing energy sources and sinks in plates using power flow maps computed from laser vibrometer measurements," *Shock and Vibration*, Bd. 5, Nr. 4, pp. 235-253, 1998.
- [17] P. Groba, J. Ebert, T. Stoewer, C. Schaal and T. Melz, "Detection of energy sinks and sources in the vibratory field of coupled structures with fluid-structure interaction," in *Proceedings of ISMA 2016*, Leuven, Belgium, 2016.
- [18] S.F. Zettel, R. Winter, S. Marburg and M. Maeder, "Ein Ansatz zur expliziten Identifizierung von Leistungsflusspfaden in Strukturintensitätsfeldern," in *DAGA Jahrestagung für Akustik*, Hannover, Germany, 2024.
- [19] N. Tanaka, S.D., Snyder, Y., Kikushima, M., Kuroda, "Vortex structural powerflow in a thin-plate and the influence on the acoustic field," in Journal of the Acoustical Society of America, Bd. 96, Nr. 3, pp. 1563-1574, 1994.